JGR Solid Earth

RESEARCH ARTICLE
10.1029/2020JB020332

Does Low-Viscosity Fracturing Fluid Always Create Complex Fractures?

Zhiqiang Chen[1], Derek Elsworth[2], and Moran Wang[1]

[1]Department of Engineering Mechanics and CNMM, Tsinghua University, Beijing, China, [2]Department of Geosciences, EMS Energy Institute and G3 Center, The Pennsylvania State University, University Park, PA, USA

Key Points:
- A grain-scale fluid-solid coupled model is developed to evaluate fluid property effect on fracture network complexity
- A statistical method is developed to evaluate heterogeneity of rocks
- A regime map indicates that complex fracturing is promoted in the intersection of the low viscosity and high heterogeneity regions

Correspondence to:
M. Wang,
mrwang@tsinghua.edu.cn

Citation:
Chen, Z., Elsworth, D., & Wang, M. (2020). Does low-viscosity fracturing fluid always create complex fractures?. *Journal of Geophysical Research: Solid Earth*, *125*, e2020JB020332. https://doi.org/10.1029/2020JB020332

Received 3 JUN 2020
Accepted 4 SEP 2020
Accepted article online 7 SEP 2020

Abstract Lower viscosity fluids are commonly believed to be able to create more complex fractures in hydraulic fracturing; however, the mechanism remains stubbornly unclear. We use a new grain-scale model with accurate coupling of hydrodynamic forces to simulate the propagation of fluid-driven fracturing. The results clarify that fracturing fluid with a lower viscosity does not always create more complex fractures. The heterogeneity in the rock exerts the principal control on systematic evolution of fracture complexity. In homogeneous rock, low viscosity fluids result in low breakdown pressure, but viscosity exerts little influence on fracture complexity. However, in heterogeneous rock, lower viscosity can lead to more complex network of fracturing. A regime map shows the dependence of fracture complexity on the degree of rock heterogeneity where low viscosity fracturing fluid more readily permeates weak defects and creates complex fracture networks.

Plain Language Summary Hydro-fracturing is an important technique in petroleum industry to stimulate well production. Generally, it is believed that lower viscosity fluids will create more complex fractures with higher cost. The mechanism of induced more complex fracture is still not fully understood yet, which may result in uncertain expense on fluid treatments. This problem will be solved by a grain-scale numerical framework to reproduce and simulate this process. The results clarify that fracturing fluid with a lower viscosity does not always create more complex fractures. The heterogeneity in the rock exerts the principal control on systematic evolution of fracture complexity. In homogeneous rock, low viscosity fluids result in low breakdown pressure, but viscosity exerts little influence on fracture complexity. However, in heterogeneous rock, lower viscosity can lead to more complex network of fracturing. The results will improve understanding of mechanism of hydro-fracturing mechanics and therefore help to optimize the cost-benefit relationship in industrial applications.

1. Introduction

Hydraulic fracturing is an important stimulation technique in tight or unconventional reservoirs to enhance gas or oil production (Economides & Nolte, 1989; Montgomery & Smith, 2010). In this process, a significant volume of fluid (fracturing fluid) is injected into the wellbore under high pressure to fracture the rock and drastically increase the permeability of and production from the formation (Economides & Nolte, 1989). Hydraulic fracturing is a strongly coupled fluid-solid process with its efficiency depending on the properties of both the fluid and the rock. The mechanical properties and stress-state of the rock are intrinsic for a specific reservoir, so that various fracturing fluids have been used to achieve different fracturing outcomes—principally related to a desired increase in fracture complexity (Barati & Liang, 2014; Wanniarachchi et al., 2017). High viscosity fluids such as cross-linked gels are typically used due to their capacity to effectively transport proppants (Wanniarachchi et al., 2017). Such fracturing fluids typically result in a single bi-wing planar crack as described by classical theories of hydraulic fracturing (Fisher et al., 2002). The single bi-wing planar fracture is suitable for reservoirs with moderate permeability, which is equivalent to increasing the length or surface area of the wellbore. However, in ultralow permeability reservoirs, such as gas shales, a simple planar fracture may be ineffective—it cannot provide large contact area with the reservoir and reduced diffusive pathway lengths and fails to improve productivity (Fisher et al., 2002; Mayerhofer et al., 2010). For example, Barnett Shale was rendered commercially successful by a shift in fracturing fluids in 1998 (Fisher et al., 2004). A blend of water with friction reducers (slickwater) was able to generate more complex fracture networks and yield economically viable production of gas (Mayerhofer et al., 1997). After that "water fracs" and the concept of "Stimulated Reservoir Volume" (meaning extremely complex

fracture network) were widely accepted (Mayerhofer et al., 2006, 2010). The development of hydraulic fracture operations indicates that fracturing fluid has a significant effect on the fracture complexity. This effect is usually qualitatively attributed to the fluid viscosity, but the direct quantitative evidence is still lacking and the understanding of the in-depth mechanism remains insufficiently clear (Song et al., 2019). Owing to the difficulty in experimentally observing the fracturing behavior, numerical explorations are needed to reveal what happens in rock during the hydraulic fracturing process.

Generally, there are two scale levels of methods in simulating hydro-fracturing, continuum-scale and grain-scale models. Continuum-scale models are routinely applied in the design of hydraulic fracture treatments (Geertsma & De Klerk, 1969; Nordgren, 1972), where a single planar crack is usually assumed and typically exclude the potential for complex fracturing behavior (Adachi et al., 2007; Barbati et al., 2016; Detournay, 2016; Hubbert & Willis, 1957). To consider the fracture network, discrete fracture network (DFN) model is widely used to predict the hydro-fracturing in unconventional reservoirs. Li and Zhang (2019) simulated the gases fracturing by DFN and found CO_2 can induce more complex fracture network than water (Li & Zhang, 2019). However, in DFN models, the fracture information (such as fracture direction, length, and amount) should be preset, and the complex fracturing behavior in rock (such as branching and fracture-fracture interaction) is difficult to be described. As an alternative, the grain-scale models are developed to explore the further mechanisms (Al-Busaidi et al., 2005; Galindo-Torres et al., 2013; Shimizu et al., 2011), among which the discrete element method (DEM) (Cundall & Strack, 1979; Galindo-Torres et al., 2012) is a promising one. Different from the traditional materials such as metals, rocks are "discontinuous" materials, comprising grains, pores, and pre-existing flaws, so that its fracturing behavior is peculiar and complex. DEM directly represents the grain-scale structure of rocks by treating rock grains as DEM particles and can hence capture the complex fracturing of rocks automatically.

In this work, a LBM-DEM coupled model (Chen et al., 2016; Chen & Wang, 2017; Galindo-Torres, 2013; Wang et al., 2016) is used to explore why different fluids result in different fracturing behaviors, and a particular focus is on the role of viscosity on evolving fracture complexity. In this model, the rock deformation and fracturing behavior is described by DEM, while the fluid flow is simulated via solving the Navier-Stokes equations by the lattice Boltzmann method (LBM), to overcome the limitation of Darcy's law in this process. Darcy's law is strictly valid to the condition creep flow at low Reynold number, but may break down during the hydro-fracturing owing to the high fluid velocity. We introduce this grain-scale numerical method in section 2, which combines the lattice Boltzmann method (LBM), the discrete element method (DEM), and an improved immersed moving boundary (IMB) method for accurate calculation of solid-fluid interaction. We then apply this method to explore the evolution of fracture complexity and the mechanism when rock heterogeneity and fluid viscosity variation are considered.

2. Grain-Scale Numerical Models for Hydro-Mechanical Coupling

Discrete element methods (DEM) are popular in simulating the mechanical behavior of granular system such as sands, soils, and rocks (Chen et al., 2018; Cundall & Strack, 1979; Damjanac & Cundall, 2016; Galindo-Torres et al., 2012). In DEM, materials are discretized as assemblies of discrete bonded particles where the mechanical behavior is obtained by tracking movements of each particle by integrating Newton's Second Law in time. The external force acting on the DEM particles includes two parts: the contact force and the cohesive force. The current numerical framework is based on the open source software MechSys (http://mechsys.nongnu.org/index.shtml) developed by Galindo-Torres (2013), where non-spherical particles can also be considered.

In order to consider the effects of cementation, the cohesive forces between two adjacent particles are assumed in normal ($\boldsymbol{n}$) and tangential ($\boldsymbol{t}$) directions, which are given by Galindo-Torres et al. (2013):

$$\begin{cases} \boldsymbol{F}_n^{cohe} = M_n^{cohe} A \varepsilon_n \boldsymbol{n} \\ \boldsymbol{F}_t^{cohe} = M_t^{cohe} A \varepsilon_t \boldsymbol{t} \end{cases}, \tag{1}$$

where $\boldsymbol{F}_n^{cohe}$ and $\boldsymbol{F}_t^{cohe}$ are cohesive forces, M_n^{cohe} and M_t^{cohe} are the elastic moduli of the virtual cements, ε_n and ε_t are the strains as the two adjacent faces separate, and A is the shared interface area. When the strain reaches a threshold value ε_{th},

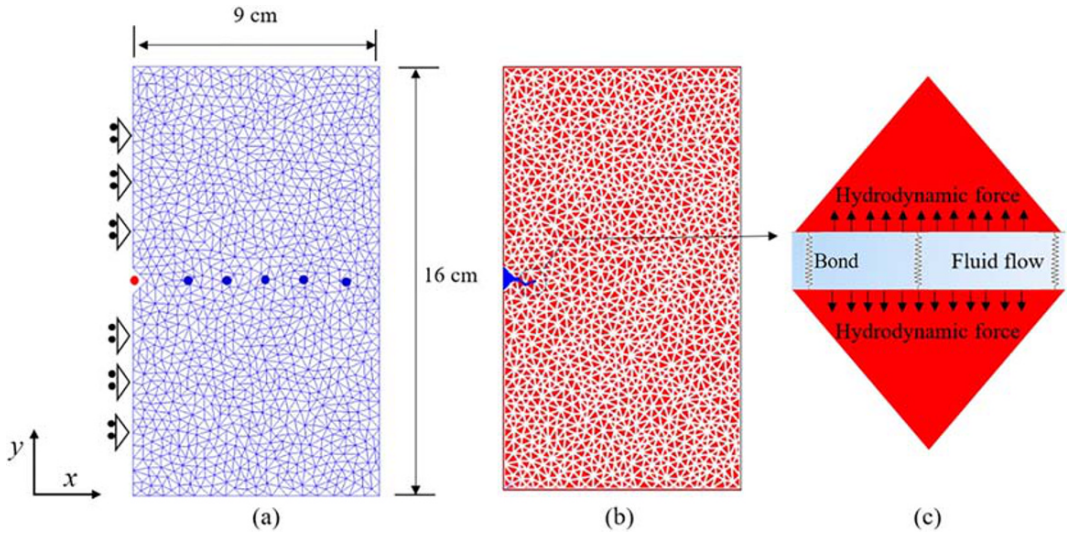

Figure 1. Schematic for LBM-DEM simulation of hydraulic fracturing. (a) Discretization of the rock matrix by triangular particles, where a borehole is set on the left edge to allow fluid injection. (b) The sizes of triangular particles in (a) are reduced by a small distance to provide flow channels (white) in the rock, where an initial crack (blue) is introduced to guide the subsequent propagation of the hydraulic fracture. (c) The diagram to show the principle of fracture propagation caused by the hydrodynamic force and torque.

$$\frac{|\varepsilon_n| + |\varepsilon_t|}{\varepsilon_{th}} > 1, \tag{2}$$

the cohesive forces will vanish, and a crack will be induced along the common interface shared by the two adjacent particles.

The second external force is the contact force when two particles collide. In the current simulation, a spring model is used:

$$\begin{cases} \boldsymbol{F}_n^{cont} = K_n \Delta l_n \boldsymbol{n} \\ \boldsymbol{F}_t^{cont} = K_t \Delta l_t \boldsymbol{t} \end{cases}, \tag{3}$$

where $\boldsymbol{F}_n^{cont}$ and $\boldsymbol{F}_t^{cont}$ are contact forces, K_n and K_t are spring stiffnesses, and Δl_n and Δl_t are the length of interpenetration in the normal and tangential directions, respectively. The efficiency of current DEM scheme in simulating mechanical behavior of rock materials can be found in our previous work (Chen, Jin, & Wang, 2018).

The lattice Boltzmann method (LBM) is a numerical method for fluid flow and makes the Navier-Stokes equations solved (Chen & Doolen, 1998). However, different from the traditional computational fluid dynamics (CFD) methods, the basic variable in LBM is the density distribution function rather than more usual macroscopic parameters (such as pressure and velocity). Here, a three-dimensional 15-speed model (D3Q15) is applied (see Figure A1) (Wang & Chen, 2007; Zhang & Wang, 2017), where the evolution equation is written as

$$f_i(\boldsymbol{x} + \boldsymbol{e}_i\delta_t, t + \delta_t) = f_i(\boldsymbol{x}, t) - \frac{1}{\tau}(f_i(\boldsymbol{x}, t) - f_i^{eq}(\boldsymbol{x}, t)), \quad i = 0\tilde{}14, \tag{4}$$

where f_i is the density distribution function in the ith discrete velocity direction $\boldsymbol{e}_i$, f_i^{eq} is the corresponding equilibrium distribution function, and δ_t is the time step. The parameter τ is the dimensionless relaxation time which is related to the fluid kinematic viscosity:

$$\nu = \frac{(\tau - 1/2)\delta_x^2}{3\delta_t}, \tag{5}$$

where δ_x is the grid size. In the D3Q15 model, the discrete velocity $\boldsymbol{e}$ has 15 directions:

Table 1
Parameters in DEM and LBM Models

Parameters	Value
Normal stiffness, K_n	1×10^8 N/m
Tangential stiffness, K_t	1×10^8 N/m
Particle friction coefficient, μ_{fric}	0.4
Normal elastic modulus, M_n^{cohe}	2.0×10^9 Pa
Tangential elastic modulus, M_t^{cohe}	4.17×10^9 Pa
Rock matrix bonding strength, ε_{th}	0.01
Fluid density, ρ	1×10^3 kg/m^3
Lattice size in LBM, δ_x	1.0×10^{-4} m
Time step in LBM, δ_t	2.0×10^{-7} s
Average particle size	5 mm

$$\boldsymbol{e} = c\begin{bmatrix} 0 & 1 & 0 & -1 & 0 & 0 & 0 & 1 & 1 & 1 & 1 & -1 & -1 & -1 & -1 \\ 0 & 0 & 0 & 0 & 0 & -1 & 1 & -1 & -1 & 1 & 1 & -1 & -1 & 1 & 1 \\ 0 & 0 & 1 & 0 & -1 & 0 & 0 & 1 & -1 & -1 & 1 & 1 & -1 & -1 & 1 \end{bmatrix}, \tag{6}$$

where $c = \delta_x/\delta_t$. The equilibrium distribution in the ith direction is written as

$$f_i^{eq}(\rho, \boldsymbol{u}) = \rho\omega_i\left[1 + \frac{3\boldsymbol{e_i}\cdot\boldsymbol{u}}{c^2} + \frac{9(\boldsymbol{e_i}\cdot\boldsymbol{u})^2}{2c^4} - \frac{3\boldsymbol{u}\cdot\boldsymbol{u}}{2c^2}\right], \tag{7}$$

where the weighting factors are

$$\omega_i = \begin{cases} 2/9, & i = 0 \\ 1/9, & i = 1-6 \\ 1/72, & i = 7-14 \end{cases}. \tag{8}$$

The fluid density and velocity are calculated as

$$\rho = \sum_i f_i, \tag{9}$$

$$\rho\boldsymbol{u} = \sum_i f_i\boldsymbol{e}_i, \tag{10}$$

and the pressure p is given by

$$p = \frac{1}{3}\rho c^2. \tag{11}$$

The immersed moving boundary (IMB) has been applied to facilitate fluid solid interaction in the previous LBM-DEM coupled models (Galindo-Torres, 2013; Noble & Torczynski, 1998; Wang et al., 2016) because of its easy implementation and high efficiency. IMB gives accurate boundary conditions to LBM for fluid flow and provides accurate forces from fluids to solid to DEM. For IMB in LBM, the fluid exists both inside (internal fluid) and outside (external fluid) of the solid particles. To ensure an accurate boundary condition for the external fluid, the internal fluid moves rigidly with the solid particle. The no-slip boundary condition is achieved by introducing a collision term Ω for the internal fluid in the standard LBM evolution equation

$$f_i(\boldsymbol{x} + \boldsymbol{e}_i\delta_t, t + \delta_t) = f_i(\boldsymbol{x}, t) - (1 - B)\frac{1}{\tau}(f_i(\boldsymbol{x}, t) - f_i^{eq}(\boldsymbol{x}, t)) + B\Omega_i^s. \tag{12}$$

The parameter Ω is the fluid-solid interaction term, which is calculated by the bounce-back for the non-equilibrium part of the density distribution

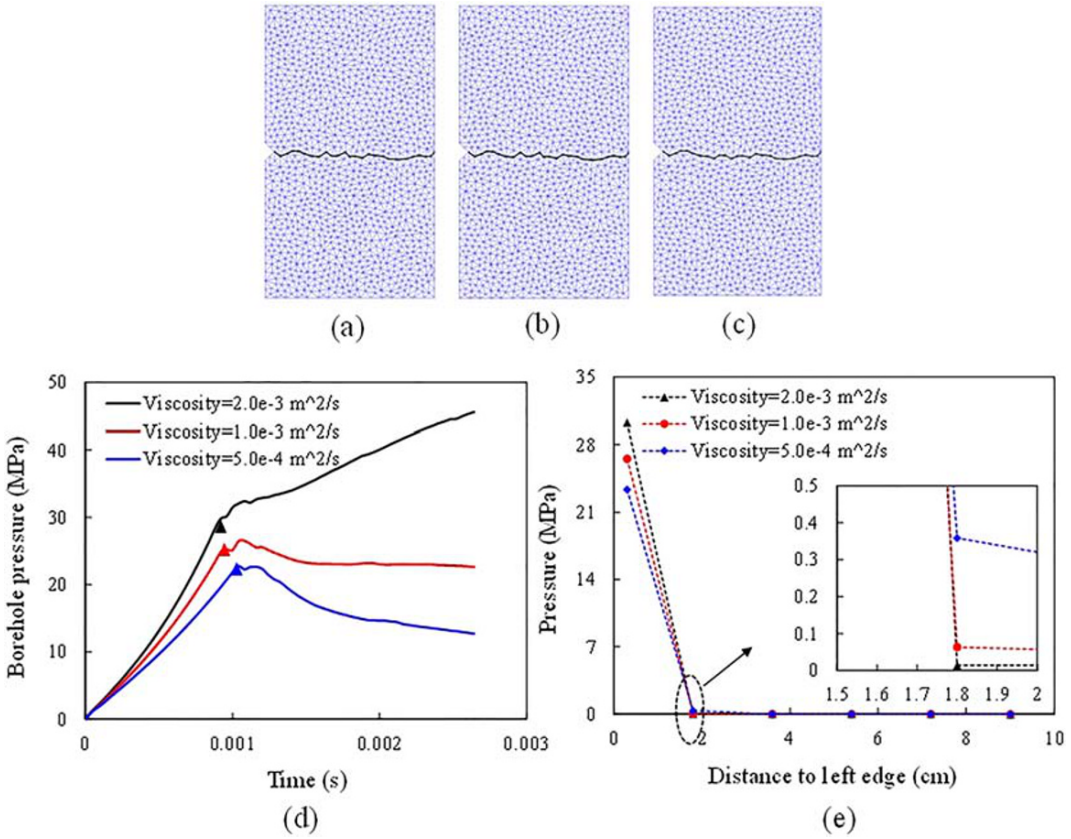

Figure 2. Hydraulic fracture evolution for fluids with contrasting viscosities. (a, b, and c) Fracture geometries for kinematic viscosities of $\nu = 2 \times 10^{-3}$ m^2/s, 1×10^{-3} m^2/s, and 5×10^{-4} m^2/s, respectively. (d) Pressure evolution in the borehole (red point in Figure 1a) during the hydraulic fracturing process. (e) Pressure distribution when the fracture is initially induced.

$$\Omega_i^s = \left[f_{-i}(\boldsymbol{x}, t) - f_{-i}^{eq}(\rho, \boldsymbol{v}_p)\right] - \left[f_i(\boldsymbol{x}, t) - f_i^{eq}(\rho, \boldsymbol{v}_p)\right], \tag{13}$$

where $\boldsymbol{v}_p$ is the DEM particle velocity at position $\boldsymbol{x}$. Weighting factor B is a function of the dimensionless relaxation time (τ) and solid volume fraction (γ) of the internal fluid at position $\boldsymbol{x}$ occupied by the particle and is given as

$$B = \frac{\gamma(\tau - 0.5)}{(1-\gamma) + (\tau - 0.5)}. \tag{14}$$

In the original IMB, the no-slip boundary condition was well established, but the hydrodynamic force calculated by this method was insufficiently accurate (Chen et al., 2013) because the inertial force of the internal fluid was ignored. To overcome this limitation, an improved IMB method (Chen, 2020) is adopted in this work, and the hydrodynamic force $\boldsymbol{F}$ and torque $\boldsymbol{T}$ are given by

$$\boldsymbol{F} = \rho_f V \frac{\boldsymbol{u_s}(t) - \boldsymbol{u_s}(t - \delta_t)}{\delta_t} - \sum_n \sum_i \frac{\delta_x^3 B_n}{\delta_t} \Omega_i^s \boldsymbol{e_i}, \tag{15}$$

$$\boldsymbol{T} = I_f \frac{\boldsymbol{\varpi_s}(t) - \boldsymbol{\varpi_s}(t - \delta_t)}{\delta_t} - \sum_n \left(\sum_i \frac{\delta_x^3 B_n}{\delta_t} \Omega_i^s \boldsymbol{e_i} (\boldsymbol{x_n} - \boldsymbol{x_{cm}}) \right). \tag{16}$$

Compared with the original IMB method, the internal fluid correction (the first term on the right-hand side of Equations 15 and 16) is added to correct the hydrodynamic force calculation, which reflects the inertial force of the internal fluid. Parameters: V is the volume of the solid particle, $\boldsymbol{u_s}$ and $\boldsymbol{\varpi_s}$ are the linear and

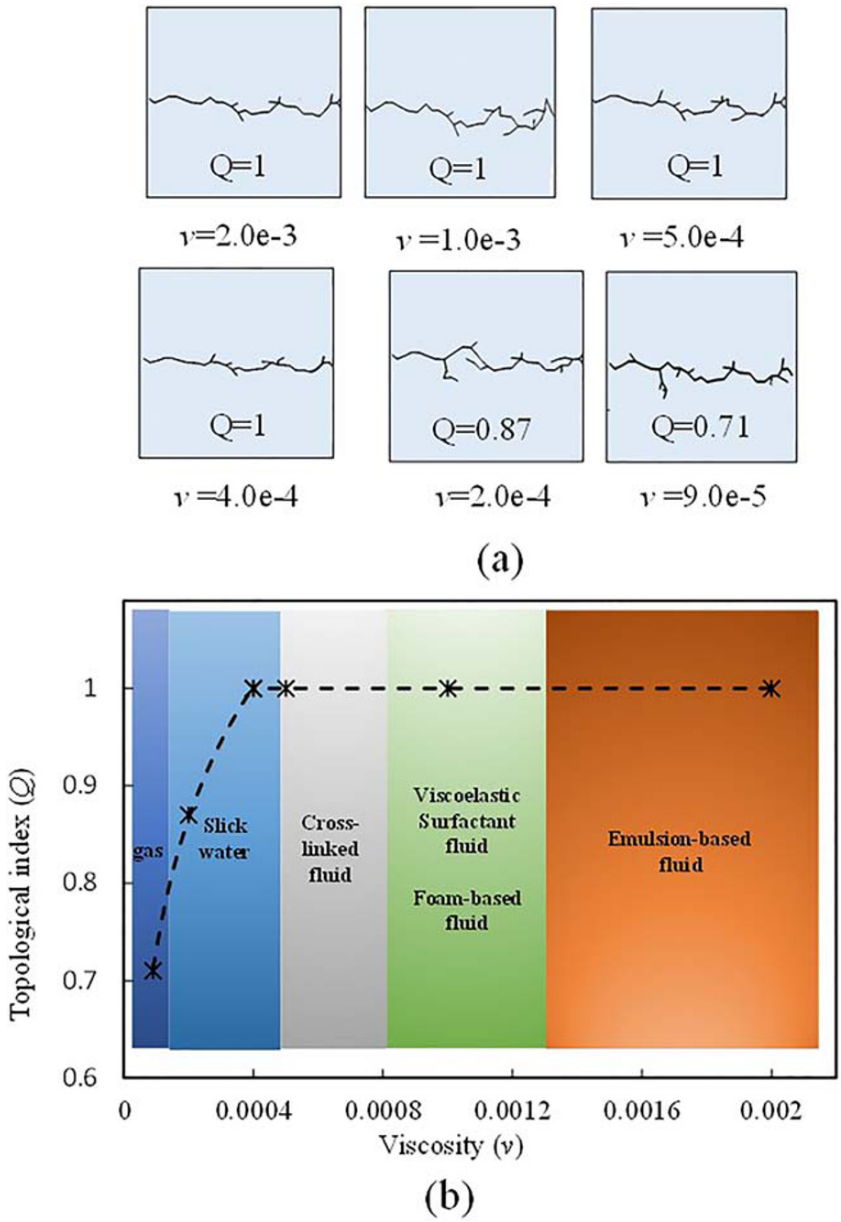

Figure 3. Evolution of a hydraulic fracture in heterogeneous samples. (a) Fracture geometry induced by fluid with viscosity of $\nu = 2 \times 10^{-3}$ m^2/s, 1×10^{-3} m^2/s, 5×10^{-4} m^2/s, 4×10^{-4} m^2/s, 2×10^{-4} m^2/s, and 9×10^{-5} m^2/s, respectively. (b) Modified topological index representing the various cases—quantitatively indicates that lower viscosity fluids result in more complex fracture networks in heterogeneous rock.

angular velocities of the DEM particle, respectively, I_f is the moment of inertia for the internal fluid covered by the DEM particle, which is calculated by the moment of inertia for the particle (I_s) as $I_f = \frac{\rho_f}{\rho_s} I_s$, $\boldsymbol{x}_n$ is the fluid cell position, and $\boldsymbol{x}_{cm}$ is the mass center of the DEM particle. The validations of this revised LBM-DEM model are given in the Appendices A.1–A.3.

3. Physical Model and Numerical Results

The physical model of this work is shown in Figure 1, where the rock matrix is discretized as an assembly of triangular particles bonded with each other (see Figure 1a). Fluid is injected into a hole from the left side of

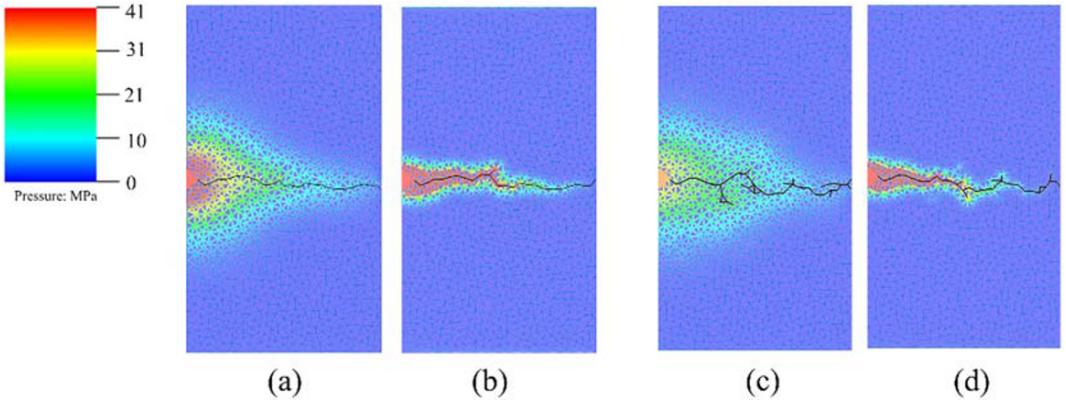

Figure 4. Pressure distribution in rock samples. Pressure distribution when the fracture is induced in the homogeneous rock ($h = 0.12$) with (a) low viscosity fluid (2×10^{-4} m^2/s) and (b) high viscosity fluid (2×10^{-3} m^2/s). Pressure distribution when the fracture is induced in the highly heterogeneous rock ($h = 0.52$) with (c) low viscosity fluid (2×10^{-4} m^2/s) and (d) high viscosity fluid (2×10^{-3} m^2/s).

the domain with a constant flowrate. A small perforation (6.5 mm) in the $\boldsymbol{x}$ direction is introduced to guide the subsequent hydraulic fracture (see Figure 1b). The sizes of triangular particles in Figure 1a are reduced by a small distance to provide flow channels (white part in Figure 1b) within the assemblage. Fluid flows only within these channels (simulated by LBM) with the hydrodynamic force imposed on the interior triangular particles calculated by the improved IMB method. These ensemble fluid forces result in propagation of the discrete hydraulic fracture. In order to capture the effects of the newly formed fracture on flow conductivity a fracture-dependent flow conductivity is applied. When the bond is intact, a high virtual solid volume (γ in Equation 14) is introduced in the flow channel, corresponding to a low conductivity. Once the bond is broken, γ in the corresponding flow channel is set to zero (Wang et al., 2011) and the flow conductivity is determined by the fracture aperture. During the hydro-fracturing simulation, the LBM node state (covered or uncovered by DEM particles) is checked in every time step. When the distance between two particles (fracture aperture) change, the number of LBM lattice will also change which determines the flow conductivity in a created fracture.

In the current simulation, the hydrodynamic force and torque (driving force) calculated by IMB are transferred to DEM particles as presented in Figure 1c. When the hydrodynamic force and torque is high enough to reach the fracturing criterion (Equation 2), the bond between two particles will be broken, and a new crack is formed. Thus, the orientation of the created fractures depends both on the interactive forces (tensile and shear force) and the strength threshold ($\underline{\varepsilon}_{th}$) of bond between two particles. The purpose of this work is to investigate the fluid viscosity effect on the fracture complexity, so that to avoid the influence from the confining stresses the samples are unconfined in current model. More details of this LBM-DEM scheme for hydraulic fracture propagation can be found in our previous work (Chen et al., 2018; Chen & Wang, 2017).

During the simulation, the left edge of the computational domain is set as a symmetric boundary, with the DEM particles to the left fixed in the x-direction but free to displace in the y-direction. The rock sample is unconfined on other three edges. In order to explore why different fluids potentially generate different fracturing behaviors, various viscosity fluids are injected. Parameters represented in the DEM and LBM models are listed in Table 1. The current DEM model is an isotropic structure and is suitable for sandstone. With the parameters in Table 1 the current model can successfully reproduce the fracturing behavior of rock (Figure A2), but no attempt has been made to match the exact macro-mechanical properties of one kind of sandstone. We may be allowed to do this, because the present objective is to show how the fracturing fluid influences the fracture complexity so that the consequent conclusions could be universally applicable with no limitation to any rock with specific macro-properties.

Figure 2 shows the resulting hydraulic fracture driven by different viscosity fluids, where (a), (b), and (c) are fracture geometries for kinematic viscosities of $\nu = 2 \times 10^{-3}$ m^2/s, 1×10^{-3} m^2/s, and 5×10^{-4} m^2/s, respectively. As presented in Figure 1b (blue part), a small perforation (6.5 mm) in the $\boldsymbol{x}$ direction is

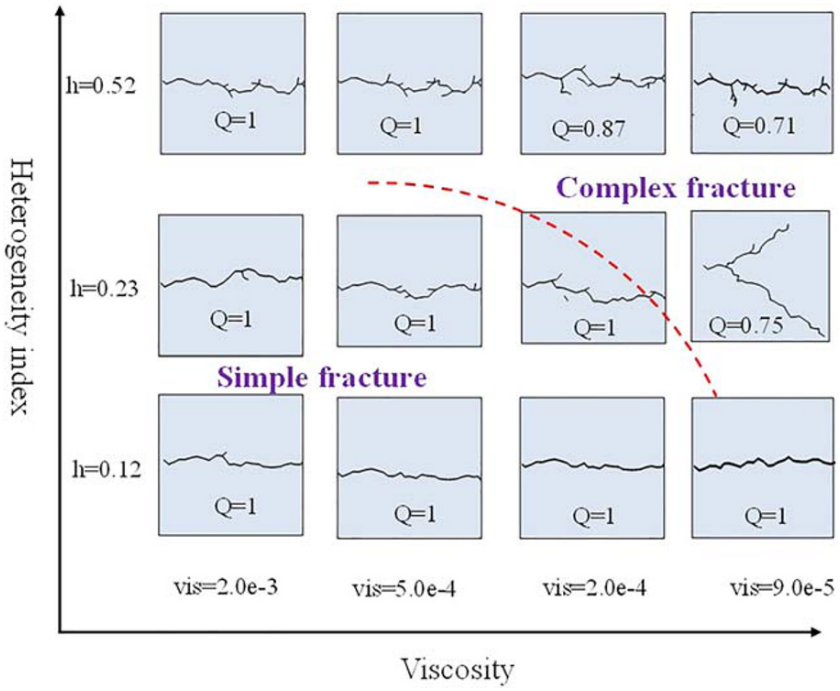

Figure 5. Regime map showing the distribution of fracture complexity (Q) in a (h, γ) diagram. Complex fractures fall at the intersection of regions of high heterogeneity and low viscosity. Simple fractures are favored for reduced heterogeneity and elevated viscosity.

introduced to the hole, which guides the subsequent hydraulic fracture to propagate along the positive direction of ***x***-axis. Figure 2d is the pressure evolution in the borehole (red point in Figure 1a) during the progress of the hydraulic fracturing, and Figure 2e is the pressure distribution when the fracture is initially induced, as measured along the central part of the computational domain (1 red point and 5 blue points in Figure 1a).

The evolution of pressure in the borehole is an important indicator of hydraulic fracture propagation. The first pressure drop represents the initiation of the fracture—referenced as the breakdown pressure. Figure 2d shows that the pressure increases most rapidly for a higher viscosity and slowest for low viscosity with the breakdown pressure also reducing with a reduction in viscosity. Similar results have also been observed in other experimental and numerical studies (Chitrala et al., 2012; Gan et al., 2015; Wang et al., 2018). In order to explain this phenomenon, the pressure distribution along the rock sample is plotted when the fracture is initially induced (Figure 2e). The leftmost points in Figure 2e are the breakdown pressure for different viscosity fluids. For the low viscosity cases, the breakdown pressure is low although the pore pressure directly adjacent to the hole is high. High pore pressure reduces the effective stress and promotes weakening of the borehole wall. The high pore pressure in the rock matrix for the low viscosity fluid can be attributed to two reasons. First, fluid with low viscosity more easily penetrates the rock matrix owing to the low flow resistance. Second, the pressure buildup for low viscosity case is slow (Figure 2d), so fluid has more time to increase the pore pressure adjacent to the borehole wall.

However, these current simulations seem to suggest that viscosity has little effect on fracture geometry. The hydraulic fractures induced by the different fluids are near identical (see Figures 2a–2c), and a thorough-going simple fracture is generated in all samples. However, previous experimental results show that the fluid viscosity is an important parameter affecting the fracture geometry (Bennour et al., 2015). When high viscosity fluid is used, such as oil, a simple fracture is formed. However, when the fluid viscosity is low, a complex fracture geometry can be induced. Thus, further discussing is needed to deal with this inconsistency.

4. Discussions

In the prior simulations, the rock sample is homogeneous, with bond strengths uniformly distributed. However, the strength heterogeneity is an important feature of rock owing to the different mineral components. This strength heterogeneity may be quantitatively represented as a Weibull distribution (McClintock & Zaverl, 1979). Thus, the impact of strength heterogeneity may be considered, by setting the bonding strength threshold (ε_{th}) as a random field following the Weibull distribution:

$$f(\varepsilon_{th}) = \frac{m}{\varepsilon_{th}^0}\left(\frac{\varepsilon_{th}}{\varepsilon_{th}^0}\right)^{m-1}\exp\left(-\left(\frac{\varepsilon_{th}}{\varepsilon_{th}^0}\right)^m\right), \tag{17}$$

where ε_{th}^0 is the average bond strength threshold and $m > 0$ is the shape parameter describing the degree of dispersion of ε_{th}. In the current work, more than 3,000 DEM particles are used, which is considered sufficiently to represent the Weibull distribution (Rossi & Richer, 1987). In order to quantify the degree of heterogeneity, an index (h) between 0 and 1 is proposed, representing the normalized standard deviation of the Weibull distribution as

$$h = \frac{\sigma_{std}}{E_{mean}} = \frac{\sqrt{\Gamma(1+2/m) - (\Gamma(1+1/m))^2}}{\Gamma(1+1/m)}, \tag{18}$$

where Γ is the gamma function, σ_{std} is the standard deviation, and E_{mean} is the mean of the distribution. When $m = 1$, $h = 1$, and this corresponds to a highly heterogeneous system. Conversely, $h = 0$ represents a totally homogeneous sample.

Figure 3 shows the evolution of the hydraulic fracture in a highly heterogeneous rock sample ($h = 0.52$ a common value used in the simulation to consider the heterogeneity effect of rock), where (a) is the fracture geometry induced by fluids with different viscosities. The fracture geometry induced by a low viscosity (9×10^{-5} m^2/s) fluid is more complex than that induced by a high viscosity (2×10^{-3} m^2/s) fluid.

In order to provide a quantitative comparison of fracture complexity induced by different fluids, a modified topological index (Q) is calculated for each case. The parameter Q is an index to quantify the complexity of the resulting fracture geometry ($0 < Q < 1$) with a lower Q corresponding to a more complex fracture geometry (Chen & Wang, 2017). The definition of the modified topological index (Montgomery & Smith, 2010) is provided in the Appendix A.4.

With the help of "modified topological index, Q," although the fracture geometry may be not completely identical under different DEM particles, the underlying physics obtained by analyzing the "topologic index" are not influenced by the specific mesh size. Figure 3b shows that for low viscosity fluids the topological index Q is smaller, which quantitatively demonstrates that in heterogeneous rock low viscosity is conducive to the formation of complex fracture network, similar to experimental observations (Bennour et al., 2015). Thus, fracturing fluid effects on fracture complexity depends on the rock properties. In homogeneous rock, fluid viscosity has little effects on fracture complexity, but in heterogeneous rock, lower viscosity may result in more complex fracture networks. In order to explain this rock-dependent effect, the pressure distribution in the rock sample when the fracture is induced is plotted in Figure 4.

Low viscosity fluid readily penetrates the rock matrix and elevates pore pressure around the main fracture (see Figures 4a and 4c). In heterogeneous rock ($h = 0.52$), the weak bonds close to the main fracture are readily broken by the high induced pore pressure (low viscosity injection), allowing the nucleation of cracks. These nucleated cracks connect to the main fracture and form a connective branch (see Figure 4c), generating the nucleus of a nascent complex fracture network. However, in homogeneous rock, bond strengths are uniformly distributed with no weak bonds existing to form such crack nucleation and branches. Thus, although low viscosity fluid can result in high pore pressures in homogeneous samples, the generation of complex fracture networks is impeded.

In summary, it is the degree of heterogeneity of the rock that controls the impact of fluid viscosity on the ensuing fracture complexity. In homogeneous samples, fluid viscosity does not affect the fracture

complexity, just as the prediction in continuum-based models. However, in heterogeneous samples, a lower viscosity fluid results in the development of more complex fracture networks—consistent with experimental observations in real rock.

To probe the evolution of fracture complexity under different conditions, the impacts of heterogeneity and viscosity are explored by systematically varying both heterogeneity ($h = 0.12$, 0.23, and 0.52) and viscosity ($\nu = 2 \times 10^{-3}$ m^2/s, 5×10^{-4} m^2/s, 2×10^{-4} m^2/s, and 9×10^{-5} m^2/s) to explore the parameter space. Figure 5 is a regime map showing fracture complexity (Q) as a function of that (h, ν) parameter space. The evolution of complex fractures falls at the intersection of the higher heterogeneity and lower viscosity regions. Conversely, simple fractures evolve for the lower heterogeneity and higher viscosity cases. For each heterogeneity index h, a critical viscosity exits, below which the transition from a simple crack to a complex fracture network occurs. This critical viscosity increases with an increase of the degree of heterogeneity of the rock. Thus, if a complex hydraulic fracture network is desired, then two key points should be noted. First, a necessary condition exists such that the degree of heterogeneity of the rock must be high—such as in reservoirs rich with natural fractures. And second, networks of complex fractures are maximally promoted where a fracturing fluid with a low viscosity is utilized, such as in "gas fracturing."

5. Conclusions

In this study, a grain-scale LBM-DEM coupled model is applied to simulate the evolution of hydraulic fractures with a focus on why different fluids result in different fracturing behaviors. To improve the accuracy of the hydrodynamic force calculation, an improved IMB method is applied. The fluid viscosity impacts fracturing behavior only through the level of heterogeneity of the rock. In homogeneous rock, fluid viscosity only impacts the breakdown pressure (low viscosity corresponding to low breakdown pressure) to initiate a fracture but exerts little influence on the ensuing fracture complexity (a similar simple fracture is induced no matter what kind of fluid is used). Conversely, in heterogeneous rock, fluid viscosity significantly impacts fracture complexity, with lower viscosity fluids resulting in more complex fracture networks. This is contributed by the presence of weak bonds (representing natural fractures or weak defects) present near the main fracture, which are easily broken by the invading high pore pressure and form discrete fracture branches. The low viscosity fluid promotes the ready buildup of pore pressures in the rock matrix enabling a complex fracture network to be more readily induced. A regime map showing the fracture complexity (Q) distribution in an (h, ν) diagram is presented, which indicates that complex fracturing is promoted in the intersection of the low viscosity and high heterogeneity regions. Thus, rock properties (heterogeneity) and fluid properties (viscosity) are two key factors governing the evolution of fracture complexity during hydraulic fracture treatments. Thus, in unconventional reservoirs, the development of complex fracture networks from heterogeneous reservoirs probed by lower viscosity fluids may increase both the rate and absolute recovery of the hydrocarbon resource.

Appendix A: Method Validations

In this part, current hydro-mechanical coupled framework is validated, including lattice Boltzmann method in simulating the fluid flow, discrete element method in describing the fracturing behavior of rock, and the improved immersed boundary method in calculating the hydrodynamic force.

A.1 Validation of Lattice Boltzmann Method

To test the LBM part, the fluid flow in a two-dimensional channel is simulated by the current D3Q15 model (see Figure A1 (c)). The physical model is presented in Figure A1 (a), where L and H is the length and width of the channel, respectively, and a periodic boundary condition is applied in the $\boldsymbol{z}$ direction. A pressure difference ΔP is applied in the Y direction. In the equilibrium state, fluid velocity distribution in the X direction can be obtained analytically:

$$u = \frac{1}{2\mu}\frac{\Delta P}{L}\left[\frac{H^2}{4} - \left(x - \frac{H}{2}\right)^2\right]. \tag{A1}$$

Figure A1 (b) shows the comparison between the analytical solution and numerical results, and good agreement is obtained.

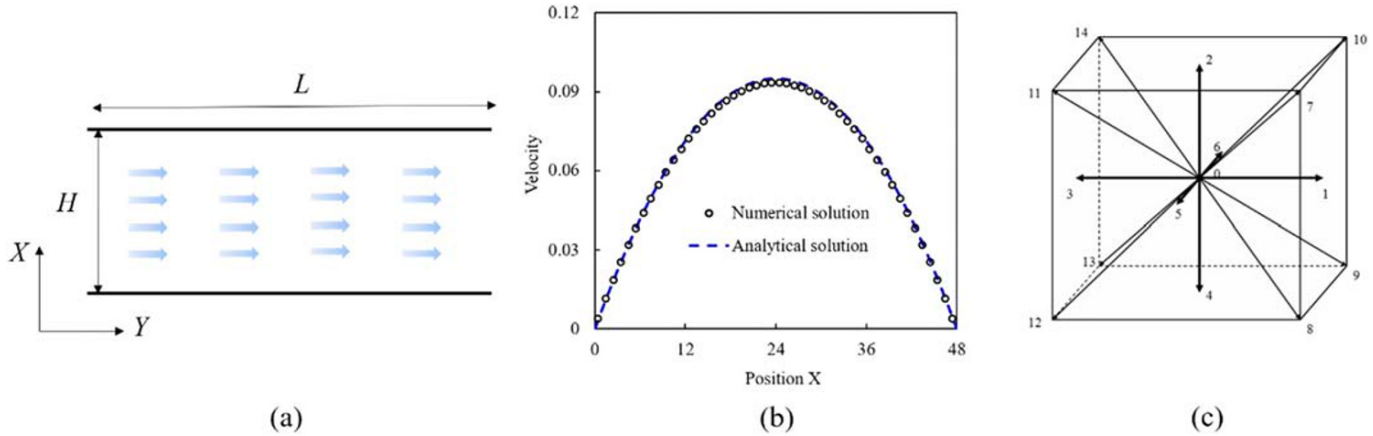

Figure A1. (a) Physical model of LBM simulation of fluid flow along a two-dimensional channel, where L and H is the length and width of the channel respectively. A pressure difference is applied in Y direction to drive the fluid motion. (b) Comparison between analytical solution and numerical result, which shows that good agreement is obtained. (c) The diagram for the D3Q15 model applied in the current simulation.

A.2 Validation of Discrete Element Method

To validate the current DEM model in capturing the fracturing behavior of rock, Brazilian test is simulated, where a disc sample, discretized into a collection of triangle particles (see Figure A2 (a)), is compressed along the direction parallel to its diameter. Figure A2 (b) shows the disc is split into two halves along the diameter, which is the typical feature of Brazilian test. The stress-strain relation during the compression process is also recorded, and the slope and peak value in Figure A2 (c) corresponds to the elasticity modulus and tensile strength, respectively. More validations of the fracturing simulation of rock with current DEM have been made by the developers, and the readers can refer to the work (Behraftar et al., 2017).

A.3 Validation of Improved Immersed Moving Boundary

In hydro-mechanical coupled model, a key point is the accurate calculation of the hydrodynamic force imposed on the solid surface. In this part, a single elliptical particle sedimentation in the Newtonian fluid is simulated to validate current improved IMB method. The physical model is presented in Figure A3 (a), where a and b are the length of the semiminor and semimajor axis of the elliptical particle, respectively. The width of channel is 0.4 cm, and the length is long enough (12 cm) to avoid the boundary influence. The particle is initially placed at the position (1.2 cm, 0.2 cm) with $\alpha = 3\pi/4$. A constant gravity force in the x direction is applied on the particle, which determines the terminal particle Reynolds number ($Re = Vb/\nu$). In this case, the terminal particle Reynolds number is equal to 6.6. The particle trajectory obtained with different methods is shown in Figure A3 (b). Current model agrees well with the FEM results in Ref. (Xia et al., 2009), but the deviation exists in previous one. Thus, current improved IMB model can give the accurate calculation of hydrodynamic force applied on the solid surface.

In order to test current model in the 3-D cases, a sphere sedimentation in a closed channel owing to the gravity acceleration (9.8 m/s^2) is simulated by the current new IMB model (see Figure A4(c)), and the numerical results are compared with the experimental ones (Cate et al., 2002). The closed channel is $100 \times 100 \times 160$ mm, and a sphere, with radius at 7.5 mm and density at 1,120 kg/m^3, is initially placed at the position (50, 50, 32.5) mm. The fluid density and viscosity are equal to 960 kg/m^3 and 0.058 Ns/m^2, respectively. In the current simulation, the domain is divided into $200 \times 200 \times 320$ lattice. The no-slip boundary condition is applied for the side walls, and the fluid velocity on the top and bottom boundaries is set to zero. Simulation results are shown in Figure A4, where the experimental results in (Cate et al., 2002) are cited for the comparison. Current new IMB method agrees with the experimental data, but a large deviation exists when using the original IMB method.

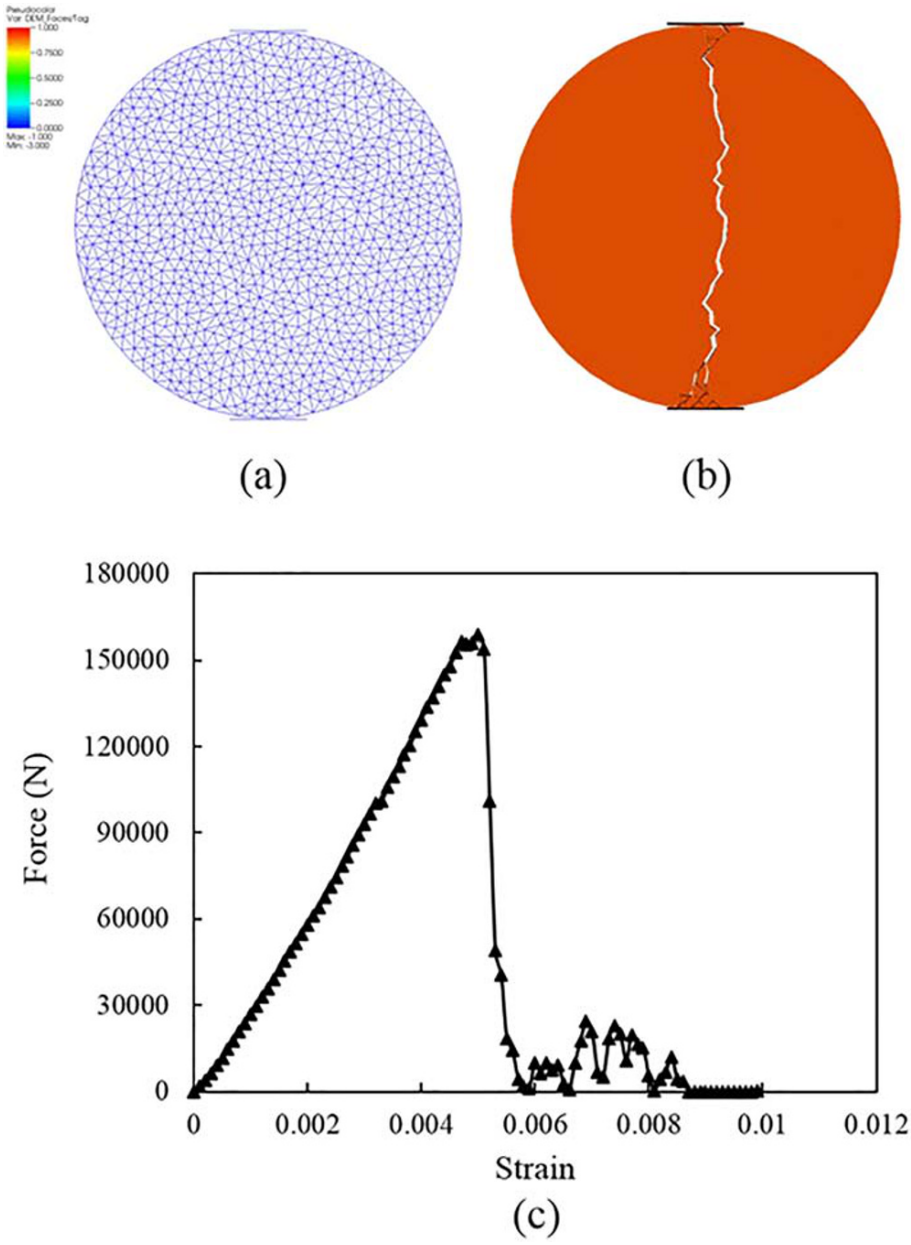

Figure A2. (a) Physical model of Brazilian test simulation, where the disc sample is discretized into a collection of triangle particles, which is compressed along the diameter. (b) The resulting fracture after the Brazilian test, which shows that current DEM model successfully captures the main feature of the fracturing behavior of rock. (c) Stress-strain relation during the compression process, where the slope and peak value corresponds to the elasticity modulus and tensile strength, respectively.

A.4 Modified Topological Index Q

The modified topological index (Q) is such a parameter between 0 and 1 to quantify the branching patterns between the two extremes, dichotomous and herringbone branching. Herringbone branching is a simple structure with low degree of the branching development. On the contrary, dichotomous branching corresponds to a high degree of the branching growth, and is regarded as an ideal hydraulic fracture with high geometric complexity. When $Q = 0$, the fracture corresponds to the dichotomous branching. When $Q = 1$, an exact herringbone branching is formed. The modified topological index (Q) is written as

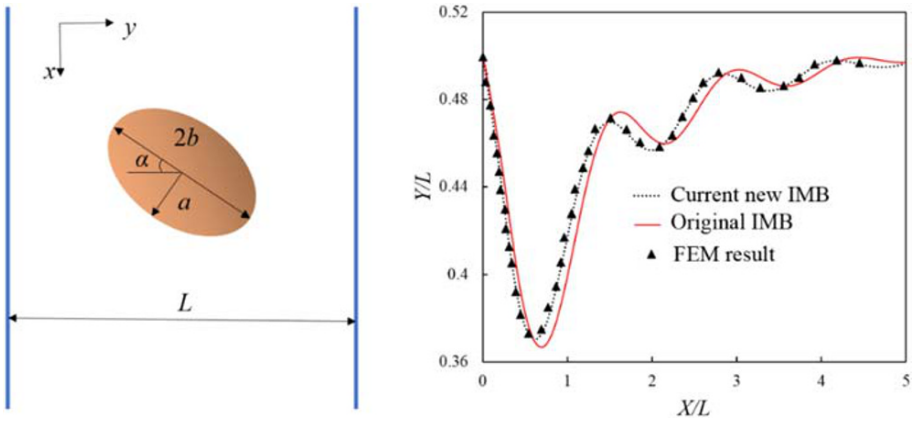

Figure A3. (a) Physical model of an elliptical particle sedimentation in the Newtonian fluid, where *a* and *b* is the length of the semiminor and semimajor axis of the elliptical particle, respectively. A constant gravity force is applied on the particle to drive its motion in the *x* direction. (b) The particle trajectory obtained with different methods, which shows that current model agrees well with the FEM results in ef. (Xia et al., 2009), but the deviation exists in previous one.

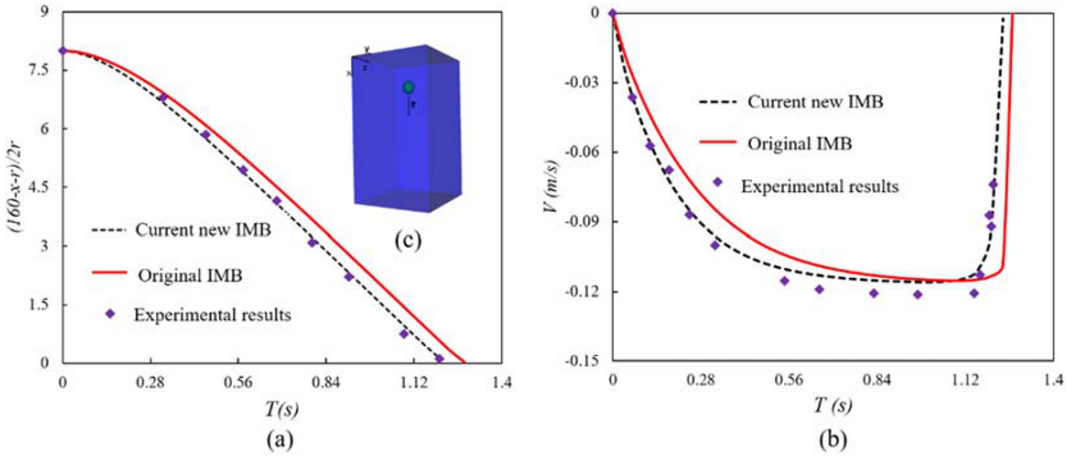

Figure A4. Comparison of (a) particle position and (b) velocity in *x* direction, where results obtained by the experiment (Cate et al., 2002) are cited to validate the current new IMB model in 3-D cases. (c) The physical model for the current 3-D simulation case.

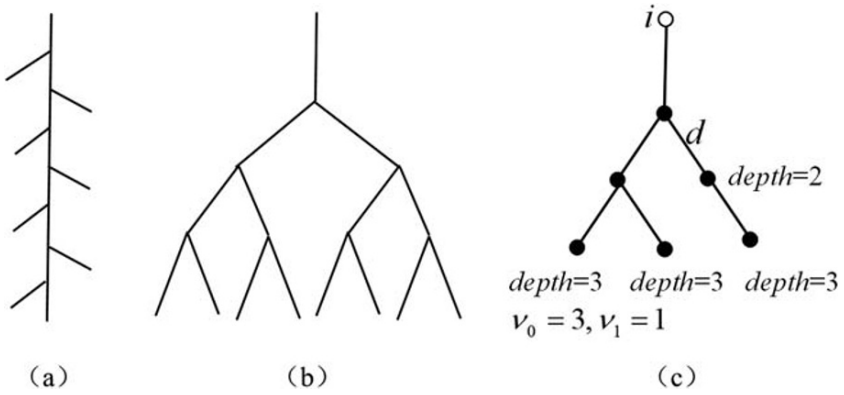

Figure A5. (a) The diagram of herringbone branching corresponding to a low degree of branching growth. (b) The diagram of dichotomous branching, which is an ideal hydraulic fracture geometry with high complexity. (c) A diagram of nonbinary tree structure.

$$q_m = \frac{b_m - b_m^{\min}}{b_m^{\max} - b_m^{\min}}, \quad b_m^{\min} = \frac{\ln(\nu_0 + 0.5\nu_1)}{\ln 2} - 1, \quad b_m^{\max} = \frac{\nu_0 + 1}{2} + 1 - \frac{1}{\nu_0} + \nu_1 + \frac{(\nu_1 + 1)\nu_1}{2\nu_0} \tag{A2}$$

where ν_0 is the number of external vertices (with outdegree 0), ν_1 the number of vertices with outdegree 1, and b_m the average topological depth.

Conflict of Interest

There is no conflict of interest in this work.

Data Availability Statement

According to AGU's Data Policy, we declare no data used in this work.

Acknowledgments

This work is financially supported by the National Natural Science Foundation of China (NSFC) (11761131012 and U1837602). The simulations are run on the "Explorer 100" cluster of Tsinghua National Laboratory for Information Science and Technology.

References

Adachi, J., Siebrits, E., Peirce, A., & Desroches, J. (2007). Computer simulation of hydraulic fractures. *International Journal of Rock Mechanics and Mining Sciences*, *44*(5), 739–757. https://doi.org/10.1016/j.ijrmms.2006.11.006

Al-Busaidi, A., Hazzard, J., & Young, R. (2005). Distinct element modeling of hydraulically fractured Lac du Bonnet granite. *Journal of Geophysical Research*, *110*, B06302. https://doi.org/10.1029/2004JB003297

Barati, R., & Liang, J. T. (2014). A review of fracturing fluid systems used for hydraulic fracturing of oil and gas wells. *Journal of Applied Polymer Science*, *131*, 40735. https://doi.org/10.1002/app.40735

Barbati, A. C., Desroches, J., Robisson, A., & McKinley, G. H. (2016). Complex fluids and hydraulic fracturing. *Annual Review of Chemical and Biomolecular Engineering*, *7*(1), 415–453. https://doi.org/10.1146/annurev-chembioeng-080615-033630

Behraftar, S., Torres, S. G., Scheuermann, A., Williams, D. J., Marques, E. A. G., Avarzaman, H. J. J. C., & Geotechnics (2017). A calibration methodology to obtain material parameters for the representation of fracture mechanics based on discrete element simulations. *Computers and Geotechnics*, *81*, 274–283. https://doi.org/10.1016/j.compgeo.2016.08.029

Bennour, Z., Ishida, T., Nagaya, Y., Chen, Y., Nara, Y., Chen, Q., et al. (2015). Crack extension in hydraulic fracturing of shale cores using viscous oil, water, and liquid carbon dioxide. *Rock Mechanics and Rock Engineering*, *48*(4), 1463–1473. https://doi.org/10.1007/s00603-015-0774-2

Cate, A. T., Nieuwstad, C. H., Derksen, J. J., & Den Akker, H. E. A. V. J. P. O. F. (2002). Particle imaging velocimetry experiments and lattice-Boltzmann simulations on a single sphere settling under gravity. *Physics of Fluids*, *14*(11), 4012–4025.

Chen, S., & Doolen, G. D. (1998). Lattice Boltzmann method for fluid flows. *Annual Review of Fluid Mechanics*, *30*(1), 329–364. https://doi.org/10.1146/annurev.fluid.30.1.329

Chen, Y., Cai, Q., Xia, Z., Wang, M., & Chen, S. (2013). Momentum-exchange method in lattice Boltzmann simulations of particle-fluid interactions. *Physical Review E*, *88*, 013303. https://doi.org/10.1103/PhysRevE.88.013303

Chen, Z. (2020). Pore-scale simulation and analysis for hydro/thermal fracturing in rock, Tsinghua university, PhD thesis.

Chen, Z., Jin, X., & Wang, M. (2018). A new thermo-mechanical coupled DEM model with non-spherical grains for thermally induced damage of rocks. *Journal of the Mechanics and Physics of Solids*, *116*, 54–69. https://doi.org/10.1016/j.jmps.2018.03.023

Chen, Z., & Wang, M. (2017). Pore-scale modeling of hydromechanical coupled mechanics in hydrofracturing process. *Journal of Geophysical Research: Solid Earth*, *122*, 3410–3429. https://doi.org/10.1002/2017JB013989

Chen, Z., Xie, C. Y., Chen, Y., & Wang, M. (2016). Bonding strength effects in hydro-mechanical coupling transport in granular porous media by pore-scale modeling. *Computation*, *4*, 15. https://doi.org/10.3390/computation4010015

Chen, Z., Yang, Z., & Wang, M. (2018). Hydro-mechanical coupled mechanisms of hydraulic fracture propagation in rocks with cemented natural fractures. *Journal of Petroleum Science and Engineering*, *163*, 421–434. https://doi.org/10.1016/j.petrol.2017.12.092

Chitrala, Y., Sondergeld, C., & Rai, C. (2012). Acoustic emission studies of hydraulic fracture evolution using different fluid viscosities, 46th US Rock Mechanics/Geomechanics Symposium.

Cundall, P. A., & Strack, O. D. (1979). A discrete numerical model for granular assemblies. *Geotechnique*, *29*(1), 47–65.

Damjanac, B., & Cundall, P. (2016). Application of distinct element methods to simulation of hydraulic fracturing in naturally fractured reservoirs. *Computers and Geotechnics*, *71*, 283–294. https://doi.org/10.1016/j.compgeo.2015.06.007

Detournay, E. (2016). Mechanics of hydraulic fractures. *Annual Review of Fluid Mechanics*, *48*(1), 311–339. https://doi.org/10.1146/annurev-fluid-010814-014736

Economides, M. J., & Nolte, K. G. (1989). *Reservoir stimulation*. NJ: Prentice Hall Englewood Cliffs.

Fisher, M., Heinze, J., Harris, C., Davidson, B., Wright, C., & Dunn, K. (2004). Optimizing horizontal completion techniques in the Barnett shale using microseismic fracture mapping, SPE Annual Technical Conference and Exhibition. https://doi.org/10.2118/90051-MS

Fisher, M. K., Wright, C. A., Davidson, B. M., Goodwin, A., Fielder, E., Buckler, W., & Steinsberger, N. (2002). Integrating fracture mapping technologies to optimize stimulations in the Barnett Shale, SPE annual technical conference and exhibition. https://doi.org/10.2118/77441-MS

Galindo-Torres, S., Pedroso, D., Williams, D., & Li, L. (2012). Breaking processes in three-dimensional bonded granular materials with general shapes. *Computer Physics Communications*, *183*(2), 266–277. https://doi.org/10.1016/j.cpc.2011.10.001

Galindo-Torres, S. A. (2013). A coupled discrete element lattice Boltzmann method for the simulation of fluid-solid interaction with particles of general shapes. *Computer Methods in Applied Mechanics and Engineering*, *265*, 107–119. https://doi.org/10.1016/j.cma.2013.06.004

Galindo-Torres, S. A., Pedroso, D. M., Williams, D. J., & Muhlhaus, H. B. (2013). Strength of non-spherical particles with anisotropic geometries under triaxial and shearing loading configurations. *Granular Matter*, *15*(5), 531–542. https://doi.org/10.1007/s10035-013-0428-6

Gan, Q., Elsworth, D., Alpern, J., Marone, C., & Connolly, P. (2015). Breakdown pressures due to infiltration and exclusion in finite length boreholes. *Journal of Petroleum Science and Engineering*, *127*, 329–337. https://doi.org/10.1016/j.petrol.2015.01.011

Geertsma, J., & De Klerk, F. (1969). A rapid method of predicting width and extent of hydraulically induced fractures. *Journal of Petroleum Technology*, *21*(12), 1571–1581. https://doi.org/10.2118/2458-PA

Hubbert, M. K., & Willis, D. G. (1957). Mechanics of hydraulic fracturing. *Transactions of the AIME*, *75*(1), 153–166.

Li, S., & Zhang, D. (2019). How effective is carbon dioxide as an alternative fracturing fluid? *SPE Journal*, *24*(02), 857–876. https://doi.org/10.2118/194198-PA

Mayerhofer, M., Richardson, M., Walker, R. Jr., Meehan, D., Oehler, M., & Browning, R. Jr. (1997). Proppants? We don't need no proppants, SPE Annual Technical Conference and Exhibition, https://doi.org/10.2118/38611-MS

Mayerhofer, M. J., Lolon, E., Warpinski, N. R., Cipolla, C. L., Walser, D. W., & Rightmire, C. M. (2010). What is stimulated reservoir volume? *SPE Production & Operations*, *25*(01), 89–98. https://doi.org/10.2118/119890-PA

Mayerhofer, M. J., Lolon, E. P., Youngblood, J. E., & Heinze, J. R. (2006). Integration of microseismic-fracture-mapping results with numerical fracture network production modeling in the Barnett Shale, SPE annual technical conference and exhibition. https://doi.org/10.2118/102103-MS

McClintock, F., & Zaverl, F. (1979). An analysis of the mechanics and statistics of brittle crack initiation. *International Journal of Fracture*, *15*(2), 107–118.

Montgomery, C. T., & Smith, M. B. (2010). Hydraulic fracturing: History of an enduring technology. *Journal of Petroleum Technology*, *62*(12), 26–40. https://doi.org/10.2118/1210-0026-JPT

Noble, D. R., & Torczynski, J. R. (1998). A lattice-Boltzmann method for partially saturated computational cells. *International Journal of Modern Physics C*, *09*(08), 1189–1201. https://doi.org/10.1142/S0129183198001084

Nordgren, R. (1972). Propagation of a vertical hydraulic fracture. *Society of Petroleum Engineers Journal*, *12*(04), 306–314. https://doi.org/10.2118/3009-PA

Rossi, P., & Richer, S. (1987). Numerical modelling of concrete cracking based on a stochastic approach. *Materials and Structures*, *20*(5), 334–337. https://doi.org/10.1007/BF02472579

Shimizu, H., Murata, S., & Ishida, T. (2011). The distinct element analysis for hydraulic fracturing in hard rock considering fluid viscosity and particle size distribution. *International Journal of Rock Mechanics and Mining Sciences*, *48*(5), 712–727. https://doi.org/10.1016/j.ijrmms.2011.04.013

Song, X., Guo, Y., Zhang, J., Sun, N., Shen, G., Chang, X., et al. (2019). Fracturing with Carbon Dioxide: From Microscopic Mechanism to Reservoir Application. *Joule*, *3*(8), 1913–1926. https://doi.org/10.1016/j.joule.2019.05.004

Wang, J., Elsworth, D., Wu, Y., Liu, J., Zhu, W., & Liu, Y. (2018). The influence of fracturing fluids on fracturing processes: A comparison between water, oil and SC-CO 2. *Rock Mechanics and Rock Engineering*, *51*(1), 299–313. https://doi.org/10.1007/s00603-017-1326-8

Wang, M., & Chen, S. (2007). Electroosmosis in homogeneously charged micro- and nanoscale random porous media. *Journal of Colloid and Interface Science*, *314*(1), 264–273. https://doi.org/10.1016/j.jcis.2007.05.043

Wang, M., Feng, Y., & Wang, C. (2016). Coupled bonded particle and lattice Boltzmann method for modelling fluid–solid interaction. *International Journal for Numerical and Analytical Methods in Geomechanics*, *40*(10), 1383–1401. https://doi.org/10.1002/nag.2481

Wang, S., Elsworth, D., & Liu, J. (2011). Permeability evolution in fractured coal: The roles of fracture geometry and water-content. *International Journal of Coal Geology*, *87*(1), 13–25. https://doi.org/10.1016/j.coal.2011.04.009

Wanniarachchi, W., Ranjith, P., & Perera, M. (2017). Shale gas fracturing using foam-based fracturing fluid: A review. *Environmental Earth Sciences*, *76*(2), 91. https://doi.org/10.1007/s12665-017-6399-x

Xia, Z., Connington, K. W., Rapaka, S., Yue, P., Feng, J. J., & Chen, S. (2009). Flow patterns in the sedimentation of an elliptical particle. *Journal of Fluid Mechanics*, *625*, 249–272. https://doi.org/10.1017/S0022112008005521

Zhang, L., & Wang, M. (2017). Electro-osmosis in inhomogeneously charged microporous media by pore-scale modeling. *Journal of Colloid and Interface Science*, *486*, 219–231. https://doi.org/10.1016/j.jcis.2016.09.057